10-16-2020

Changes in Crater Geometry Revealed by Inversion of Harmonic Infrasound Observations: 24 December 2018 Eruption of Mount Etna, Italy

Leighton M. Watson
Stanford University

Jeffrey B. Johnson
Boise State University

Mariangela Sciotto
Istituto Nazionale di Geofisica e Vulcanologia

Andrea Cannata
Istituto Nazionale di Geofisica e Vulcanologia

Geophysical Research Letters

RESEARCH LETTER
10.1029/2020GL088077

Key Points:
- Eruptive activity at Mount Etna's summit generated harmonic infrasound signals due to crater resonance
- Peak frequency of infrasound signal decreased and resonance increased after fissure eruption on flank
- Infrasound amplitude spectra can be inverted for crater shape and used to track changes in morphology

Supporting Information:
- Supporting Information S1

Correspondence to:
L. M. Watson,
lwatson2@uoregon.edu

Citation:
Watson, L. M., Johnson, J. B., Sciotto, M., & Cannata, A. (2020). Changes in crater geometry revealed by inversion of harmonic infrasound observations: 24 December 2018 eruption of Mount Etna, Italy. *Geophysical Research Letters*, *47*, e2020GL088077. https://doi.org/10.1029/2020GL088077

Received 15 APR 2020
Accepted 12 SEP 2020
Accepted article online 21 SEP 2020

Changes in Crater Geometry Revealed by Inversion of Harmonic Infrasound Observations: 24 December 2018 Eruption of Mount Etna, Italy

Leighton M. Watson[1,2], Jeffrey B. Johnson[3], Mariangela Sciotto[4], and Andrea Cannata[4,5]

[1]Department of Geophysics, Stanford University, Stanford, CA, USA, [2]Department of Earth Sciences, University of Oregon, Eugene, OR, USA, [3]Department of Geosciences, Boise State University, Boise, ID, USA, [4]Istituto Nazionale di Geofisica e Vulcanologia, Osservatorio Etneo, Catania, Italy, [5]Dipartimento di Scienze Biologiche, Geologiche e Ambientali-Sezione di Scienze della Terra, Università degli Studi di Catania, Catania, Italy

Abstract In December 2018, Mount Etna (Italy) experienced a period of increased eruptive activity that culminated in a fissure eruption on the southeast flank. After the onset of the flank eruption, the peak frequency of the summit infrasound signals decreased while resonance increased. We invert infrasound observations for crater geometry and show that crater depth and radius increased during the eruption, which suggests that the flank eruption drained magma from the summit and that eruptive activity led to erosion of the crater wall. By inverting the entire infrasound amplitude spectra rather than just the peak frequency, we are able to place additional constraints on the crater geometry and invert for, rather than assume, the crater shape. This work illustrates how harmonic infrasound observations can be used to obtain high-temporal-resolution information about crater geometry and can place constraints on complex processes occurring in the inaccessible crater region during eruptive activity.

Plain Language Summary Volcanoes generate low-frequency sound waves in the atmosphere (infrasound) that can be recorded by specialized microphones. Much like giant musical instruments, the character of the sound can depend upon the shape and size of the crater. Mount Etna erupted in December 2018 with lava flowing out a fissure on the flank of the volcano. The character of the sound changed after the flank eruption. We study the change in the character of the sound in order to estimate how the shape of the volcanic crater at the summit of Mount Etna changed. Our results show that the crater got deeper and wider, which suggests that the eruption of lava on the flank of the volcano drained magma from the summit area. This work shows how infrasound observations can track changes in crater geometry and provide insight about the magma plumbing systems beneath volcanoes.

1. Introduction

Mount Etna is an open-vent volcano on the eastern coast of Sicily (Italy) that persistently degasses and frequently erupts tephra and gas into the atmosphere (Rose et al., 2013). Eruptive activity at Mount Etna is characterized by Strombolian explosions and fire fountaining at the summit interspersed with hazardous fissure eruptions on the flanks (Allard et al., 2006; Behncke et al., 2014; De Beni et al., 2015) and occasional sub-Plinian paroxysmal eruptions (Calvari et al., 2018). The summit activity frequently generates infrasound (low-frequency acoustic waves in the atmosphere) that is characterized by harmonic peaks in the frequency domain (Cannavò et al., 2019; Sciotto et al., 2013; Spina et al., 2015).

Mount Etna experienced a period of increased eruptive activity in the second half of 2018 (Global Volcanism Program, 2018) that culminated on 24 December 2018 with the opening of a 2 km long fissure on the southeast flank (Figure 1; Cannavò et al., 2019; Laiolo et al., 2019) and intense Strombolian activity and abundant ash emissions from the summit craters (Global Volcanism Program, 2019). The eruptive fissure opened at 11:11 UTC (Cannavò et al., 2019) and generated a lava flow into Valle del Bove that covered about 1 km^2 (Global Volcanism Program, 2019). After several hours, the explosivity of the flank eruption decreased although the fissure continued to erupt effusively and fed the lava flow until 27 December. Explosive activity at the summit continued throughout the flank eruption (Cannavò et al., 2019; Global Volcanism Program, 2019; Laiolo et al., 2019).

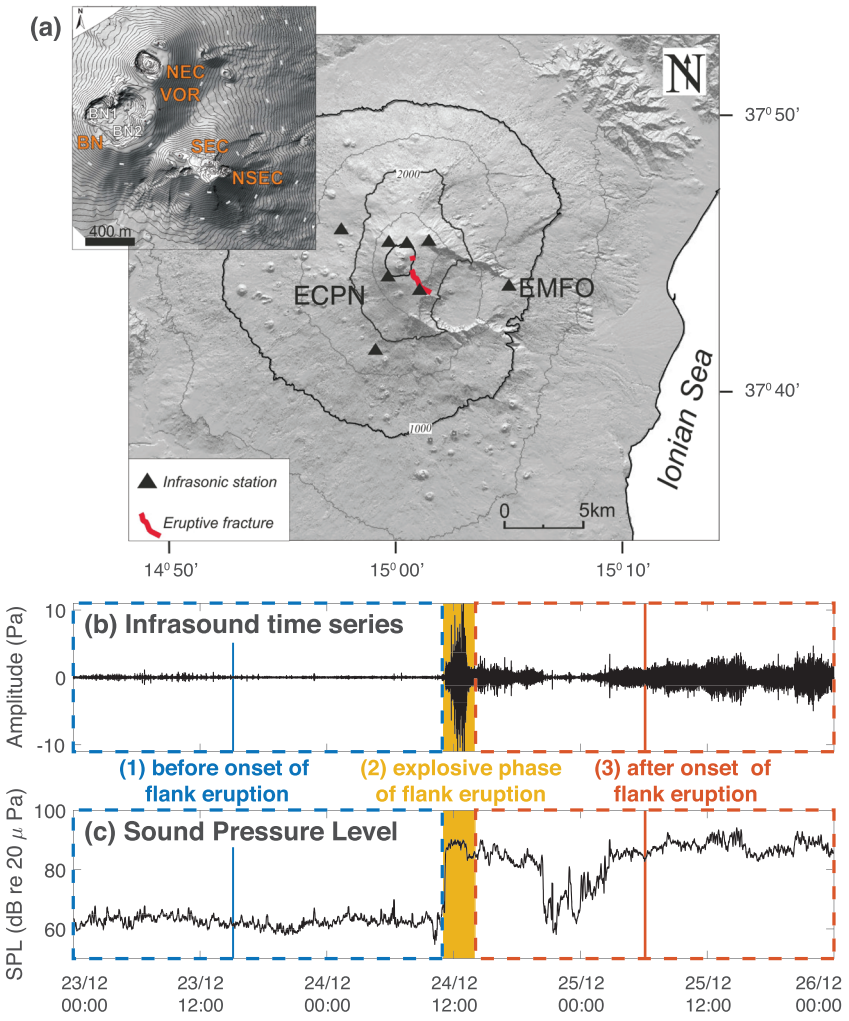

Figure 1. (a) Maps of Mount Etna showing location of infrasound sensors (black triangles) and eruptive fracture (red). Inset shows named craters (VOR, Voragine; BN, Bocca Nuova; NEC, North-East Crater; SEC, South-East Crater; NSEC, New South-East Crater; from Neri et al., 2017). Infrasound sources at the summit craters were located at BN-1 (Cannavò et al., 2019). (b) Infrasound time series recorded at station EMFO is divided into (1) before onset of flank eruption (23 December 00:00 to 24 December 11:00 UTC), (2) explosive phase of flank eruption (24 December 11:00 to 24 December 14:00 UTC), and (3) after onset of flank eruption (24 December 14:00 to 26 December 00:00 UTC). (c) Sound pressure level computed over 5 min intervals with reference pressure $p_0 = 20\ \mu$Pa. The vertical blue and red lines indicate the 15 min windows of data with high signal-to-noise ratio that are used to invert for the crater geometry.

The character of the harmonic infrasound signal changed during the eruption. The amplitude increased (Figure 1), the peak frequency decreased, and the quality factor, which can be a proxy for crater resonance, increased after the onset of flank eruption (Figure 2). Previous studies have linked crater geometry to the characteristics of harmonic infrasound signals recorded at open-vent volcanoes (e.g., Fee et al., 2010; Johnson & Watson, 2019; Johnson et al., 2018; Richardson et al., 2014; Watson et al., 2019). Following previous work at Mount Etna by Sciotto et al. (2013) and Spina et al. (2015), Cannavò et al. (2019) related the decrease in peak frequency of the infrasound observations to a decrease in the height of the magma column in the conduit. Cannavò et al. (2019) used an analytical model to relate peak frequency to the length of the approximately cylindrical conduit (Equation 2). This model is appropriate for the deep narrow conduit but is unable to fully describe the flared portion of the upper crater.

Here, we build upon the work of Cannavò et al. (2019) by extending the analysis from the peak frequency to consider the entire amplitude spectra of the infrasound observations. We use the crater acoustic resonance (CRes) model of Watson et al. (2019) to simulate the infrasound amplitude spectra for a quasi-

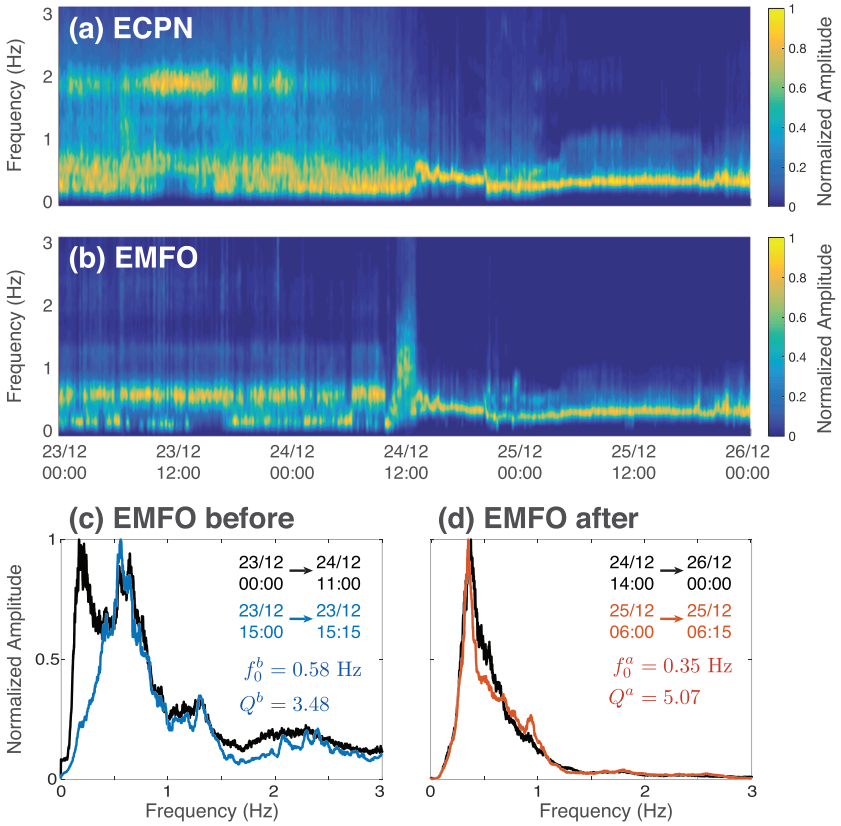

Figure 2. Spectrograms recorded at (a) Station ECPN and (b) Station EMFO. Spectrograms are computed with 5 min sliding windows and 90% overlap and are colored by normalized spectral amplitude. (c) Spectra recorded at Station EMFO for before flank eruption showing average spectra (black; 23 December 00:00 to 24 December 11:00) and spectra for a short period of high signal-to-noise ratio (SNR) (blue; 23 December 15:00 to 15:15). (d) Spectra recorded at Station EMFO for after fissure eruption showing average spectra (black; 24 December 14:00 to 26 December 00:00) and spectra for a short period of high SNR (red; 25 December 06:00 to 06:15). The timing of the blue and red spectra in (c) and (d) corresponds to the vertical lines in Figure 1b and 1c. The spectra for the two short periods of high SNR are used to invert for crater geometry.

1-D crater where the cross-sectional area can vary with depth. We invert the infrasound observations (Figures 2c and 2d) for the crater geometry before and after the onset of flank eruption to investigate how magma drainage and explosive summit activity on 24 December 2018 modified the geometry of Bocca Nuova crater.

2. Harmonic Volcano Infrasound Signals

Harmonic infrasound signals have been observed at a number of open-vent volcanoes including Cotopaxi (Ecuador; Johnson et al., 2018), Kilauea (Hawaii; Fee et al., 2010; Garcés et al., 2003), and Villarrica (Chile; Goto & Johnson, 2011; Johnson et al., 2018; Richardson et al., 2014). The harmonic nature of the infrasound signals is due to resonance of the air mass between base of the crater or the free magma surface at the top of the conduit and the crater rim (Fee et al., 2010; Goto & Johnson, 2011; Johnson & Watson, 2019; Johnson, Ruiz, et al., 2018; Johnson, Watson, et al., 2018; Richardson et al., 2014; Sciotto et al., 2013; Watson et al., 2019; Witsil & Johnson, 2018).

Although Helmholtz resonance has been suggested for other volcanoes (e.g., Fee et al., 2010; Goto & Johnson, 2011; Witsil & Johnson, 2018), it is unlikely at Mount Etna because of the absence of a constriction in the crater. Hence, we model the harmonic infrasound signals as due to acoustic resonance. Acoustic resonance occurs because acoustic waves, excited by explosions or unsteady degassing from the top of the magma column, are reflected from the crater outlet due to a contrast in the acoustic impedance between the crater

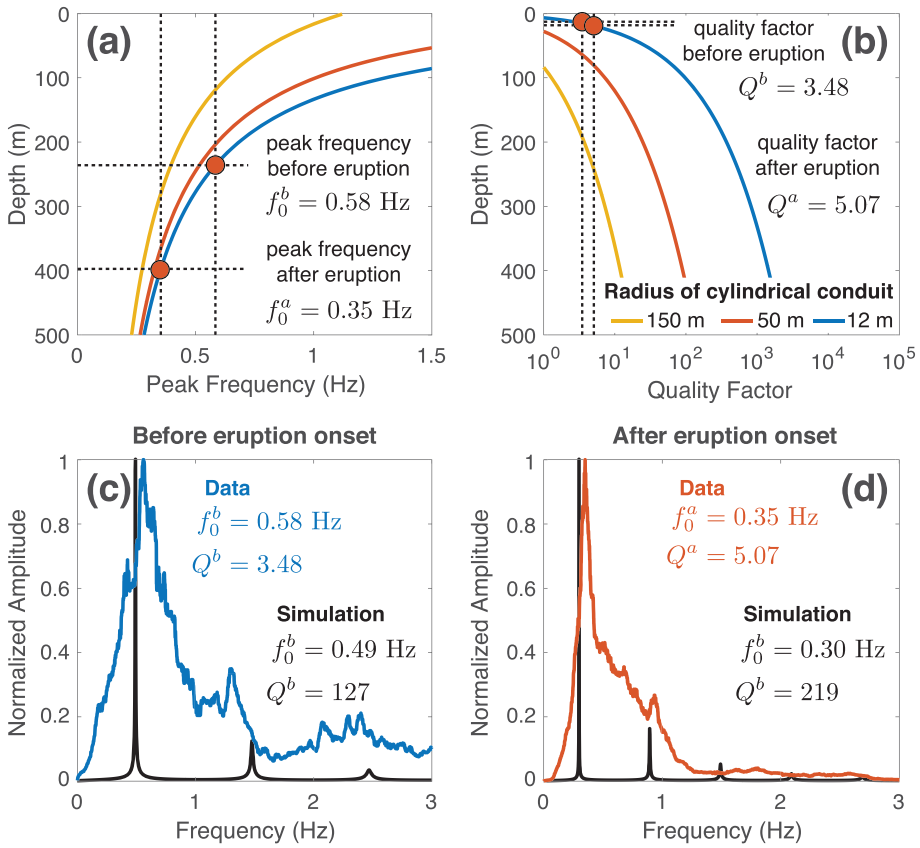

Figure 3. (a) Peak frequency calculated by Equation 2 and (b) quality factor calculated by Equation 4 as a function of depth for cylindrical craters with several different radii. Red circles indicate (a) peak frequency and (b) quality factor from the data and associated depth of cylindrical conduit with 12 m radius. (c) Infrasound spectra for 15 min window before and (d) after the onset of the flank eruption showing the infrasound signal recorded at station EMFO (blue, 23 December 15:00 to 15:15; red, 25 December 06:00 to 06:15) and the simulated spectra (black) computed with CRes. The data spectra are the same as shown in Figures 2c and 2d. The simulated spectra are calculated with a Brune source with $\sigma = 0.3$ s (Equation 6), speed of sound of 575 m/s (Cannavò et al., 2019), and a cylindrical conduit geometry with a radius of 12 m and a depth of (c) 238 m before and (d) 401 m after the onset of the flank eruption.

outlet and the atmosphere. Acoustic impedance, $Z = p/U$, is the ratio of acoustic pressure, p, to acoustic flow, U. For 1-D flow approximation, $U = vA$ where v is vertical velocity and A is cross-sectional area. Acoustic impedance provides a measure of resistance to flow; there is an impedance drop at the crater outlet because it is easier to force a parcel of air into the atmosphere than into a crater. While temperature and gas composition influence the impedance contrast at the crater outlet, the dominant control is crater geometry (Watson et al., 2019); it is harder to force air into a narrow crater than a wide crater. When the impedance contrast is high, acoustic waves are preferentially reflected from the crater outlet and form standing waves in the crater. When the impedance contrast is reduced, acoustic waves can more easily radiate into the atmosphere, which causes attenuation (Rossing & Fletcher, 2004, Chapter 8).

For a narrow cylindrical crater that is closed at the base and open at the outlet, the peak frequency, f_0, is given by

$$f_0 = \frac{c}{4L}, \tag{1}$$

where c is the speed of sound in the crater and L is the length of the resonating cavity, for example, crater depth. Equation 1 assumes a cylinder with $ka \ll 1$, where k is the wavenumber and a is the radius. When the crater radius is an appreciable fraction of the length, as is often the case for volcanic craters, $ka \sim 1$ and

end effects must be accounted for by replacing L with an effective length, L_{eff} (Johnson et al., 2018; Kinsler et al., 2000; Rossing & Fletcher, 2004):

$$f_0 = \frac{c}{4L_{\text{eff}}} \text{ where } L_{\text{eff}} = L + \frac{8a}{3\pi}, \tag{2}$$

where a is the crater radius.

An important metric that can be used to characterize harmonic infrasound signals is the quality factor, Q, which is defined as

$$Q = \frac{f_0}{\Delta f}, \tag{3}$$

where Δf is the spectral bandwidth measured as the width of the spectral peak at $1/\sqrt{2}$ of the maximum amplitude. The quality factor is inversely proportional to the amount of attenuation in the system. Attenuation occurs through the radiation of acoustic waves to the atmosphere. The quality factor depends on crater geometry due to the acoustic impedance contrast at the outlet (see Watson et al., 2019). In the frequency domain, a low-quality factor corresponds to a broad spectral peak. For a cylindrical crater, the quality factor is given by (Johnson et al., 2018; Kinsler et al., 2000; Moloney & Hatten, 2001)

$$Q = \frac{4L^2}{\pi a^2} + \frac{32L}{3\pi^2 a}. \tag{4}$$

Figures 3a and 3b show the analytical solutions for peak frequency (Equation 2) and quality factor (Equation 4) for a cylindrical conduit as a function of depth. Peak frequency decreases with increasing conduit length while quality factor increases.

3. Mount Etna Infrasound Data and the 24 December 2018 Fissure Eruption

Infrasound data at Mount Etna are recorded by a network of eight stations distributed around the volcano within 1–9 km of the summit vents (Figure 1; Cannata et al., 2013). The summit stations are strongly affected by wind noise and have issues with signal continuity, especially during the winter months. Figures 2a and 2b show two spectrograms recorded at Station ECPN, which is located near the summit, and Station EMFO, which is on the flank, respectively. Despite being closer to the eruptive activity at the summit, the signal recorded at ECPN prior to the fissure eruption is less clear than at EMFO due to strong wind noise at low frequencies. The two spectrograms are in good agreement after the fissure eruption when the amplitude of the volcanic signal is larger (Figure S1 in the supporting information). We focus on data from Station EMFO, which is located 8.1 km from Bocca Nuova crater on the east flank, as it has the best signal-to-noise ratio (SNR) and well recorded the high-frequency signal associated with the fissure eruption.

In this work we analyze infrasound data at Station EMFO recorded over a 72 hr period from 23 December 00:00 to 26 December 00:00 UTC. Each station was equipped with a GRASS 40AN microphone with a flat response at a sensitivity of 50 mV/Pa in the frequency range of 0.3–20,000 Hz and sampled at 50 Hz (Cannavò et al., 2019). The low-frequency corner of 0.3 Hz unfortunately overlaps with the frequency range of interest, and therefore, the instrument response must be corrected for. Linear trends are removed from the data, and we apply a band-pass filter with a 0.15 Hz low-frequency cutoff to remove the low-frequency noise that is added by the instrument correction and a 10 Hz high cutoff frequency.

We describe the eruption chronology as (Figure 1): (1) before flank eruption (23 December 00:00 to 24 December 11:00 UTC), (2) explosive phase of flank eruption (24 December 11:00 to 14:00 UTC), and (3) after explosive phase of flank eruption (24 December 14:00 to 26 December 00:00 UTC). Before and after the explosive phase of the flank eruption infrasound sources were localized to Bocca Nuova crater (vent BN-1), whereas during the explosive phase of the flank eruption sources were associated with the eruptive fissure as well as at BN-1 (Cannavò et al., 2019).

During the explosive phase of the flank eruption, the infrasound signal transitions to lower peak frequency, decreased spectral bandwidth, and increased quality factor (Figure 2). The spectral content of the infrasound

signal is remarkably stable before and after the flank eruption, which suggests that the signal is predominantly controlled by geometry effects rather than source effects that may vary over shorter time scales.

Figures 2c and 2d show the average spectra (black) for before and after the flank eruption, respectively. We focus on two 15 min windows of data with high SNR, before (Figure 2c, blue; 23 December 15:00 to 15:15) and after (Figure 2d, red; 25 December 06:00 to 06:15) the flank eruption that we will use to invert for the crater geometry. The 15 min spectra are in good agreement with the average spectra. The only discrepancy is that the average spectra before the flank eruption has a peak at 0.2 Hz that is not seen in the 15 min spectra. This is the microbarom peak (Bowman et al., 2005). By focusing on a short time period of high SNR, the contribution of the microbarom peak is minimized, and we reduce any microbarom contamination of the volcano signal that we are interested in.

The peak frequency observed in the infrasound data (0.58 Hz before and 0.35 Hz after) corresponds to depths of 238 m before and 401 m after the onset of the flank eruption (assuming cylindrical conduit [Equation 2] with a 12 m radius and speed of sound of 575 m/s [Cannavò et al., 2019]). The quality factor observations, however, suggest that the cylindrical crater is substantially shallower and only increased in depth from 15 m before the flank eruption to 19 m afterward (Figure 3). The discrepancy between the depths estimated from these two metrics demonstrates that a cylindrical conduit is unable to explain the observations and a more complex crater geometry is required.

4. CRes Model

Previous studies of harmonic infrasound signals from open-vent volcanoes have used analytical expressions to relate peak frequency to crater geometry (e.g., Cannavò et al., 2019; Fee et al., 2010; Richardson et al., 2014; Sciotto et al., 2013; Witsil & Johnson, 2018). These studies have been limited to simple crater geometries where analytical formula exist that relate geometry and peak frequency. Watson et al. (2019) developed a numerical model, CRes (Watson, 2019), that simulates the crater acoustic response for quasi-1-D crater geometries. CRes simulates the entire amplitude spectra and can be used to provide additional constraints on crater geometry and eruption properties. Here, we provide a brief overview of, CRes, which is described in Watson et al. (2019).

The simulated infrasound signal, Δp, is calculated by the time domain convolution of a source time function, s, described as the volume flux at the base of the crater (m^3/s), with a transfer function, T, that accounts for propagation from the base of the crater to the receiver:

$$\Delta p(t, r) = T(t, r) * s(t), \tag{5}$$

where t is time and r is the distance from the crater outlet to the receiver. The transfer function is divided into two parts: (1) crater acoustic response within the crater and (2) propagation from the crater outlet to the receiver. The crater is described as quasi-1-D (accounting for changes in cross-sectional area with depth), and wave propagation is described by linear acoustics. Acoustic radiation from the crater outlet is modeled as a baffled piston embedded in an infinite plane (Rossing & Fletcher, 2004).

Acoustic waves are excited by the volume flux at the base of the crater, such as from unsteady degassing or explosive bubble bursts. Previous studies (e.g., Johnson et al., 2018) assumed a symmetric Gaussian pulse. However, radar observations of bursting bubble surfaces (Gerst et al., 2013) and full-waveform inversion results using numerical Green's functions (Iezzi et al., 2019; Kim et al., 2015) suggest an asymmetric volume flux with a rapid onset followed by a gradual decay may be more realistic. This can be described by a Brune model (Brune, 1970):

$$s(t) = AtH(t)\exp\left(-\frac{t}{\sigma}\right), \tag{6}$$

where A is the amplitude, $H(t)$ is the Heaviside function, and σ is the width. Further discussion about the influence of the source mechanism on harmonic infrasound signals is included in Johnson et al. (2018).

We use CRes to simulate the infrasound signal for a cylindrical crater with a radius of 12 m and depth of 238 m before (Figure 3c) and 401 m after (Figure 3d) the onset of the flank eruption. The simulated infrasound

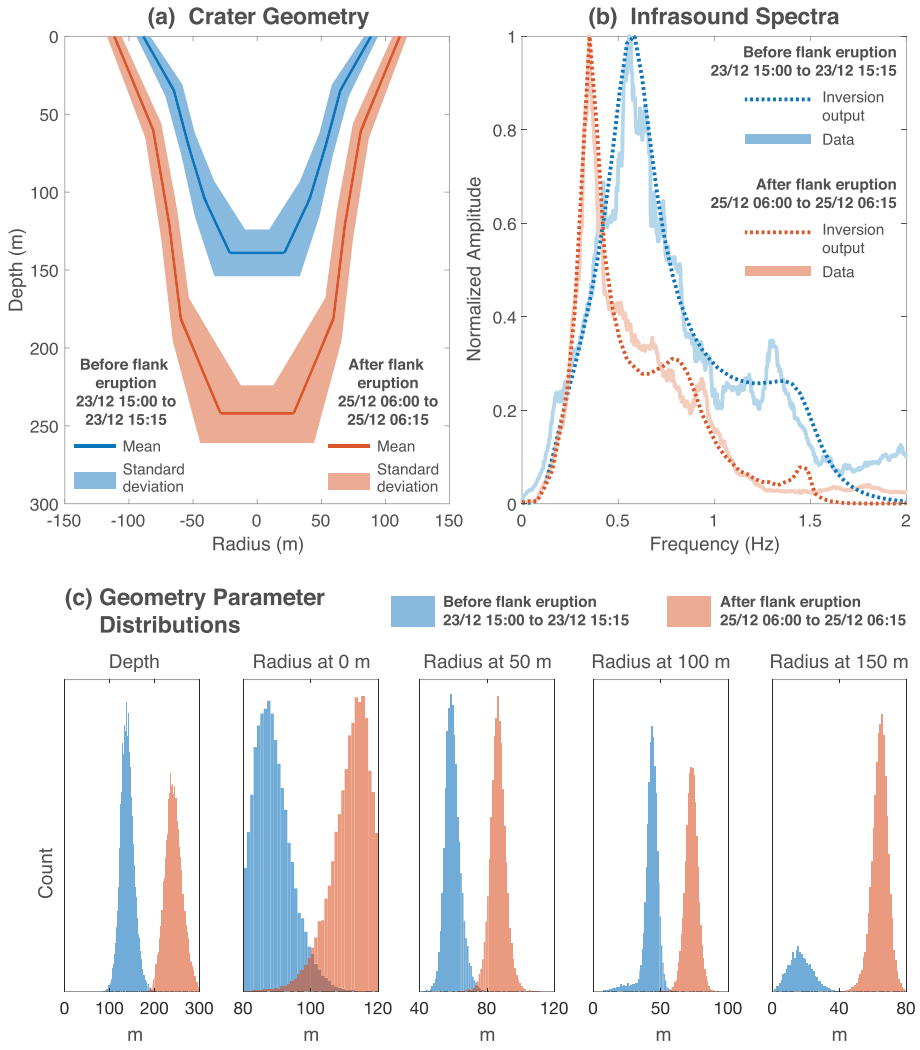

Figure 4. Inversion results for before (blue, 23 December 15:00 to 15:15) and after (red, 25 December 06:00 to 06:15) the flank eruption. (a) Inverted mean crater geometry (solid lines) showing plus/minus one standard deviation (shaded). (b) Normalized infrasound amplitude spectra showing data (solid) and the simulated spectra corresponding to the mean geometry shown in (a) (dotted). (c) Distribution of geometry parameters (depth and radii at specified depths) for before (blue) and after (red) the flank eruption.

peaks are far narrower and have higher quality factors than observed in the data. The infrasound signal for the cylindrical crater is a good match to the peak frequency but overpredicts the quality factor by 2 orders of magnitude. This suggests that the outlet of the resonating cavity is wider than 12 m and that the crater geometry is more complex than a simple cylinder.

5. Inverting for Crater Geometry

We use the inversion scheme described below to invert the harmonic infrasound observations for the crater geometry. We use CRes to simulate the infrasound signal for arbitrary quasi-1-D crater geometry and focus on two short windows when the infrasound data had a high SNR, one before (23 December 15:00 to 15:15, Figures 2c and 3c) and one after (25 December 25 06:00 to 06:15, Figures 2d and 3d) the explosive phase of the flank eruption to obtain two snapshots of the crater geometry.

The inversion scheme used here was first presented in Watson et al. (2019) and is a Markov chain Monte Carlo (MCMC) style inversion scheme. The steps for the *i*th iteration are shown below:

(1) Take a random step in all parameter directions to calculate a vector of proposed parameter values:

$$\vec{x}_i^* = \frac{\vec{x}_{i-1}}{\vec{x}_0} + \vec{h}_{i-1}\Delta x, \tag{7}$$

where $\vec{x}_i^*$ is the vector of proposed parameter values, $\vec{x}_{i-1}$ is the vector of parameter values at the previous iteration, and $\vec{x}_0$ is the initial estimate. $\vec{h}_{i-1}$ is the same dimension as $\vec{x}$ with each entry randomly sampled from the uniform distribution [−1,1] for each iteration and Δx is the scalar step size. If necessary, repeat the procedure until a value of $\vec{x}_i^*$ is chosen that satisfies the specified bounds.

(2) Simulate infrasound signal for $\vec{x}_i^*$ using CRes.

(3) Evaluate the misfit function for the proposed parameters, $M(\vec{x}_i^*)$.

(4) Accept the proposed parameters, $\vec{x}_i = \vec{x}_i^*$, if:

(a) The misfit is reduced: $M(\vec{x}_i^*) < M(\vec{x}_{i-1})$,

(b) $\gamma_i < \alpha$ where γ_i is randomly sampled from the uniform distribution [0, 1] and α is a scalar parameter, $\alpha \in [0, 1]$. This allows the inversion to escape local minima.

Otherwise, reject the proposed parameters and keep the previous solution, $\vec{x}_i = \vec{x}_{i-1}$.

These steps are repeated until the specified number of iterations is reached.

Watson et al. (2019) previously defined the misfit function as the weighted sum of the difference between the peak frequency and quality factor of the data and simulated spectra. While an intuitive choice, this misfit function has several shortcomings; it focuses entirely on the dominant peak, does not account for asymmetry, and introduces uncertainty through the choice of the weighting parameters and the method used to calculate the quality factor. Therefore, in this work we define the misfit function at iteration i as follows:

$$M(\vec{x}_i) = ||A_{\text{data}} - A(\vec{x}_i)||_2, \tag{8}$$

where A_{data} and $A(\vec{x}_i)$ are the normalized amplitude spectra of the data and the simulation, respectively, between 0 and 2 Hz. This misfit function includes all information about the spectra within the specified frequency band rather than focusing on the dominant peak and does not introduce any additional parameters. The same filtering applied to the data is applied to the synthetic spectra to ensure consistency.

The crater geometry is parameterized as a depth, L, and N radii values, r^k, that are equally spaced in depth. Hence, the parameter vector is $\vec{x_i} = [L_i, r_i^1, r_i^2, ..., r_i^N]$. The depth value evolves with each iteration, and the depth of the radii values is updated accordingly. The depths of the kth radii values at the ith iteration are given by

$$z_i^k = (k-1)\frac{L_i}{N-1}, \tag{9}$$

where L_i is the crater depth at the ith iteration and $k \in [1, \ldots, N]$. The crater geometry is linearly interpolated between the N radii values to create a crater profile that can be used to simulate the infrasound signal.

The inversions are initialized with a cylindrical crater with a depth of 200 m and a radius of 100 m (inversion results are independent of the starting model, as shown in the supporting information) and are run for 1×10^5 iterations with $\Delta x = 0.05$ and $\alpha = 0.1$. The crater outlet radius is constrained to between 80 and 120 m, based on satellite observations and digital elevation models of the summit craters (Neri et al., 2017), while the other parameters are unconstrained. The radius is not required to decrease with depth.

We assume a crater temperature of 100°C, which, for specific gas constant of 287 J kg^{-1} K^{-1} and ratio of specific heats of $\gamma = 1.4$, gives a speed of sound of 387 m/s. This is slower than the 575 m/s speed of sound used by Cannavò et al. (2019) because they focused on the deep, narrow part of the crater that is filled with hot volcanic gases whereas in this work we consider the whole crater including the flared upper portion where there is mixing between the volcanic gases and atmospheric air (we examine the influence of the crater

temperature on the inversion results in the supporting information). We prescribe the source function as a Brune model with $\sigma = 0.3$ s and acknowledge that future work may wish to explore the effects of additional source models. It is possible to invert for the crater geometry and source function simultaneously; however, without additional constraints, the inversion is unstable. The crater geometry is parameterized with $N = 5$ radii values (we examine the influence of the geometry parameterization on the inversion results in the supporting information).

The inverted crater geometry for before and after the flank eruption is shown in Figure 4a. Before the eruption, the inversion gives a mean outlet radius of 89 m and depth of 139 m with a flaring crater shape. After the eruption, the mean outlet radius increases to 112 m and the depth increases to 242 m. The simulated spectra are a good fit to the observed data (Figure 4b) and are a substantial improvement over the spectra for the cylindrical crater geometry shown in Figure 3.

Figure 4c shows the geometry distributions (depth and radii at specified depths). Distributions are predominantly Gaussian, except for the outlet radius where the parameter value is constrained between 80 and 120 m. The before and after inversion results are separated for most parameters indicating that the two solutions are substantially different. At 150 m depth, there are more samples after the flank eruption than before because most of the before solutions are shallower than 150 m.

6. Discussion

The crater became deeper after the flank eruption. The drop of the crater floor is likely due to magma draining from the summit craters during the dike intrusion and flank eruption (Cannavò et al., 2019). This suggests a connection between the summit magma reservoir and the plumbing system feeding the flank eruption. Similar connectivity has been previously observed at Kilauea (Neal et al., 2019; Patrick et al., 2019) and at Mount Etna (Spina et al., 2015).

The inversion results show that the crater also became wider after the flank eruption, which was accompanied by vigorous eruptive activity at the summit (Cannavò et al., 2019; Global Volcanism Program, 2019; Laiolo et al., 2019). We suggest two possible explanations. First, magma draining from the crater could have caused the crater walls to become unstable and collapse. Second, explosive activity could have ripped material away from the wall and erupted it out of the crater, eroding the wall and causing the crater to widen (Houghton & Nairn, 1991; Woods & Bower, 1995).

This study builds upon previous work that has used harmonic infrasound observations to infer crater geometry at open-vent volcanoes (Fee et al., 2010; Goto & Johnson, 2011; Richardson et al., 2014; Sciotto et al., 2013; Spina et al., 2015; Watson et al., 2019). Using local infrasound observations to constrain crater geometry is an useful monitoring technique; however, future work needs to use independent observations to validate the infrasound-derived estimates of crater geometry. Here, we perform a constrained inversion where the outlet radius is required to be between 80 and 120 m based on satellite observations (Neri et al., 2017). We are unfortunately unaware, at this time, of other independent observations that could be used to validate our inversion results.

We focus on two 15 min windows of infrasound data that include both explosions and tremor signals (Cannavò et al., 2019). The source mechanism of the infrasound signal likely varies during these windows and could include large to small bubbles bursting, continuous small-amplitude explosions that merge together into tremor signals, or unsteady degassing. Without additional constraints, however, we are unable to accurately model the complexity in the source. Therefore, we assume a constant source mechanism of a Brune spectra with $\sigma = 0.3$ s (Equation 6). This source has less energy at high frequencies, which may explain the misfit between the data and simulations at >1.5 Hz. The remarkable stability of the spectral content of the infrasound signal before and after the flank eruption suggests that the dominant control on the signal is geometry, which changed as a result of the flank eruption, as opposed to the source, which is likely to vary on shorter time scales.

The source function can be parameterized and included in the inversion; however, without additional constraints, inverting for the crater geometry and the source simultaneously results in an unstable inversion. Synthetic inversions of simulated infrasound signals could be used to explore parameter sensitivity and may shed light on how to invert for both geometry and source. Future studies at other open-vent

volcanoes with well-constrained crater geometry, such as Kilauea during the 2018 eruptive sequence (Neal et al., 2019; Patrick et al., 2019), could invert infrasound observations to place constraints on the source mechanism.

We model the acoustic radiation as a baffled piston in a half space. In recent years, numerous studies have shown that topographic scattering is important, even for near-field observations (Fee et al., 2017; Iezzi et al., 2019; Kim & Lees, 2011, 2014). We contend that we can neglect topographic scattering here due to the low frequencies that we consider and because the spectral content is similar across all stations in the network (Figure S1; Cannavò et al., 2019). Throughout this eruption, the topographic profile between the crater rim and Station EMFO was constant and the influence of topographic scattering outside of the crater is constant.

We note that future work, however, should take topography into account. A computationally efficient inversion could be designed by using CRes to model propagation inside the crater and a 3-D model for propagation from the crater outlet to the receiver. Outside of the crater, the topography would be assumed to be fixed. This would allow the wave propagation to be precomputed and the acoustic pressure at the receiver calculated by convolving the wave propagation transfer function with the outlet value from CRes. Therefore, the 3-D wave propagation simulation would only have to be calculated once rather than at every step in the inversion, which would be prohibitively computationally expensive. Such an approach may result in an improved fit to the data, especially at high frequencies where topographic scattering is more pronounced.

7. Conclusion

Eruptive activity at the summit craters on Mount Etna frequently generates infrasound signals that display harmonic peaks. During eruptive activity in December 2018, the character of the infrasound signal changed drastically after the onset of a flank eruption on 24 December. Previous work by Cannavò et al. (2019) related the decrease in the peak frequency to an increase in the crater depth, which they inferred to be due to the magma column at the summit dropping in response to magma erupting out the flank. Here, we invert infrasound observations for the crater geometry and use the entire infrasound amplitude spectra to place improved constraints on the crater geometry. The inversion results presented here show that the base of the crater dropped from 139 to 242 m, which supports the interpretation of Cannavò et al. (2019), and the crater outlet increased in radius from 89 to 112 m. This suggests that, in addition to magma draining from the summit, substantial erosion or collapse of destabilized crater walls may have occurred. Future work mapping the summit craters and geological observations of eruptive products could be used to validate the infrasound-derived geometry estimates presented here.

This work showcases the utility of inverting harmonic infrasound observations for crater geometry at open-vent volcanoes. Infrasound observations can frequently be made at safe distances during eruptive activity and, as illustrated here, can be used to place constraints on changes in crater geometry. Inverting the infrasound amplitude spectra enables the crater shape to be solved for whereas previous studies that only considering the peak frequency needed to assume a crater shape, such as cylindrical (Cannavò et al., 2019; Johnson et al., 2018) or a Bessel horn (Richardson et al., 2014). Using infrasound to monitor changes in crater geometry can provide insight on magma movement and eruption properties.

Data Availability Statement

In accordance with INGV's data policy, infrasound data are available online (at https://doi.org/10.13127/etna_infra/raw_20181223_25). The latest version of modeling and inversion code is hosted at GitHub (https://github.com/leighton-watson/CRes) and the version used in this manuscript is archived at https://doi.org/10.5281/zenodo.4032469.

Acknowledgments

We are indebted to the technicians of the INGV, Osservatorio Etneo, for enabling the acquisition of infrasonic data. We thank David Fee and an anonymous reviewer for their constructive comments. This work was partially supported by National Science Foundation Grants EAR-1830976 and EAR-1949219.

References

Allard, P., Behncke, B., D'Amico, S., Neri, M., & Gambino, S. (2006). Mount Etna 1993–2005: Anatomy of an evolving eruptive cycle. *Earth-Science Reviews*, *78*(1–2), 85–114. https://doi.org/10.1016/j.earscirev.2006.04.002

Behncke, B., Branca, S., Corsaro, R. A., De Beni, E., Miraglia, L., & Proietti, C. (2014). The 2011-2012 summit activity of Mount Etna: Birth, growth and products of the new SE crater. *Journal of Volcanology and Geothermal Research*, *270*(May 1971), 10–21. https://doi.org/10.1016/j.jvolgeores.2013.11.012

Bowman, J. R., Baker, G. E., & Bahavar, M. (2005). Ambient infrasound noise. *Geophysical Research Letters*, *32*, L09803. https://doi.org/10.1029/2005GL022486

Brune, J. N. (1970). Tectonic stress and the spectra of seismic shear waves from earthquakes. *Journal of Geophysical Research*, *75*(26), 4997–5009.

Calvari, S., Cannavò, F., Bonaccorso, A., Spampinato, L., & Pellegrino, A. G. (2018). Paroxysmal explosions, lava fountains and ash plumes at Etna Volcano: Eruptive processes and hazard implications. *Frontiers in Earth Science*, *6*, 107. https://doi.org/10.3389/feart.2018.00107

Cannata, A., Di Grazia, G., Aliotta, M., Cassisi, C., Montalto, P., & Patanè, D. (2013). Monitoring seismo-volcanic and infrasonic signals at volcanoes: Mt. Etna case study. *Pure and Applied Geophysics*, *170*(11), 1751–1771. https://doi.org/10.1007/s00024-012-0634-x

Cannavò, F., Sciotto, M., Cannata, A., & Di Grazia, G. (2019). An integrated geophysical approach to track magma intrusion: The 2018 Christmas Eve eruption at Mount Etna. *Geophysical Research Letters*, *46*, 8009–8017. https://doi.org/10.1029/2019gl083120

De Beni, E., Behncke, B., Branca, S., Nicolosi, I., Carluccio, R., D'Ajello Caracciolo, F., & Chiappini, M. (2015). The continuing story of Etna's New Southeast Crater (2012–2014): Evolution and volume calculations based on field surveys and aerophotogrammetry. *Journal of Volcanology and Geothermal Research*, *303*(February 2013), 175–186. https://doi.org/10.1016/j.jvolgeores.2015.07.021

Fee, D., Garcés, M., Patrick, M., Chouet, B., Dawson, P., & Swanson, D. (2010). Infrasonic harmonic tremor and degassing bursts from Halema'uma'u Crater, Kilauea Volcano, Hawaii. *Journal of Geophysical Research*, *115*, B11316. https://doi.org/10.1029/2010JB007642

Fee, D., Izbekov, P., Kim, K., Yokoo, A., Lopez, T., Prata, F., et al. (2017). Eruption mass estimation using infrasound waveform inversion and ash and gas measurements: Evaluation at Sakurajima Volcano, Japan. *Earth and Planetary Science Letters*, *480*, 42–52. https://doi.org/10.1016/J.EPSL.2017.09.043

Garcés, M., Harris, A., Hetzer, C., Johnson, J., Rowland, S., Marchetti, E., & Okubo, P. (2003). Infrasonic tremor observed at Klauea Volcano, Hawai'i. *Geophysical Research Letters*, *30*(20), 2023. https://doi.org/10.1029/2003gl018038

Gerst, A., Hort, M., Aster, R. C., Johnson, J. B., & Kyle, P. R. (2013). The first second of volcanic eruptions from the Erebus volcano lava lake, Antarctica—Energies, pressures, seismology, and infrasound. *Journal of Geophysical Research: Solid Earth*, *118*, 3318–3340. https://doi.org/10.1002/jgrb.50234

Global Volcanism Program (2018). Report on Etna (Italy) (*12*): Smithsonian Institution. https://doi.org/10.5479/si.GVP.BGVN201812-211060

Global Volcanism Program (2019). Report on Etna (Italy) (*4*): Smithsonian Institution. https://doi.org/10.5479/si.GVP.BGVN201904-211060

Goto, A., & Johnson, J. B. (2011). Monotonic infrasound and Helmholtz resonance at Volcan Villarrica (Chile). *Geophysical Research Letters*, *38*, L06301. https://doi.org/10.1029/2011GL046858

Houghton, B. F., & Nairn, I. A. (1991). The 1976–1982 Strombolian and phreatomagmatic eruptions of White Island, New Zealand: Eruptive and depositional mechanisms at a 'wet' volcano. *Bulletin of Volcanology*, *54*(1), 25–49. https://doi.org/10.1007/BF00278204

Iezzi, A. M., Fee, D., Kim, K., Jolly, A. D., & Matoza, R. S. (2019). Three-dimensional acoustic multipole waveform inversion at Yasur Volcano, Vanuatu. *Journal of Geophysical Research: Solid Earth*, *124*, 8679–8703. https://doi.org/10.1029/2018JB017073

Johnson, J. B., Ruiz, M. C., Ortiz, H. D., Watson, L. M., Viracucha, G., Ramon, P., & Almeida, M. (2018). Extraordinary infrasound tornillos produced by Volcán Cotopaxi's Deep Crater. *Geophysical Research Letters*, *45*, 5436–5444. https://doi.org/10.1029/2018GL077766

Johnson, J. B., & Watson, L. M. (2019). Monitoring volcanic craters with infrasound "music". *EOS*. https://doi.org/10.1029/2019EO123979

Johnson, J. B., Watson, L. M., Palma, J. L., Dunham, E. M., & Anderson, J. F. (2018). Forecasting the eruption of an open-vent volcano using resonant infrasound tones. *Geophysical Research Letters*, *45*, 2213–2220. https://doi.org/10.1002/2017GL076506

Kim, K., Fee, D., Yokoo, A., & Lees, J. M. (2015). Acoustic source inversion to estimate volume flux from volcanic explosions. *Geophysical Research Letters*, *42*, 5243–5249. https://doi.org/10.1002/2015GL064466

Kim, K., & Lees, J. M. (2011). Finite-difference time-domain modeling of transient infrasonic wavefields excited by volcanic explosions. *Geophysical Research Letters*, *38*, L06804. https://doi.org/10.1029/2010GL046615

Kim, K., & Lees, J. M. (2014). Local volcano infrasound and source localization investigated by 3D simulation. *Seismological Research Letters*, *85*, 1177–1186. https://doi.org/10.1785/0220140029

Kinsler, L. E., Frey, A. R., Coppens, A. B., & Sanders, J. V. (2000). *Fundamentals of acoustics* (4th ed.), vol. 1. https://doi.org/10.1002/9780470612439

Laiolo, M., Ripepe, M., Cigolini, C., Coppola, D., Della Schiava, M., Genco, R., et al. (2019). Space- and ground-based geophysical data tracking of magma migration in shallow feeding system of Mount Etna Volcano. *Remote Sensing*, *11*(10), 1182. https://doi.org/10.3390/rs11101182

Moloney, M. J., & Hatten, D. L. (2001). Acoustic quality factor and energy losses in cylindrical pipes. *American Journal of Physics*, *69*(3), 311–314. https://doi.org/10.1119/1.1308264

Neal, C. A., Brantley, S. R., Antolik, L., Babb, J. L., Burgess, M., Calles, K., et al. (2019). The 2018 rift eruption and summit collapse of Kilauea Volcano. *Science*, *363*(6425), 367–374.

Neri, M., De Maio, M., Crepaldi, S., Suozzi, E., Lavy, M., Marchionatti, F., et al. (2017). Topographic maps of Mount Etna's summit craters, updated to December 2015. *Journal of Maps*, *13*(2), 674–683. https://doi.org/10.1080/17445647.2017.1352041

Patrick, M., Orr, T., Anderson, K., & Swanson, D. (2019). Eruptions in sync: Improved constraints on Klauea Volcano's hydraulic connection. *Earth and Planetary Science Letters*, *507*, 50–61. https://doi.org/10.1016/j.epsl.2018.11.030

Richardson, J. P., Waite, G. P., & Palma, J. L. (2014). Varying seismic-acoustic properties of the fluctuating lava lake at Villarrica volcano, Chile. *Journal of Geophysical Research: Solid Earth*, *119*, 5560–5573. https://doi.org/10.1002/2014JB011002.Received

Rose, W. I., Luis Palma, J., Delgado Granados, H., & Varley, N. (2013). Open-vent volcanism and related hazards: Overview. In Rose, W. I., Luis Palma, J., Delgado Granados, H., & Varley, N. (Eds.), *Understanding open-vent volcanism and related hazards* (pp. vii–xiii): Geological Society of America Special Paper 498. https://doi.org/10.1130/2013.2498(00)

Rossing, T. D., & Fletcher, N. H. (2004). *Principles of vibration and sound* (Second), vol. 1: Springer. https://doi.org/10.1017/CBO9781107415324.004

Sciotto, M., Cannata, A., Gresta, S., Privitera, E., & Spina, L. (2013). Seismic and infrasound signals at Mt. Etna: Modeling the north-east crater conduit and its relation with the 2008–2009 eruption feeding system. *Journal of Volcanology and Geothermal Research*, *254*, 53–68. https://doi.org/10.1016/j.jvolgeores.2012.12.024

Spina, L., Cannata, A., Privitera, E., Vergniolle, S., Ferlito, C., Gresta, S., et al. (2015). Insights into Mt. Etna's shallow plumbing system from the analysis of infrasound signals, August 2007–December 2009. *Pure and Applied Geophysics*, *172*(2), 473–490. https://doi.org/10.1007/s00024-014-0884-x

Watson, L. M. (2019). CRes (Volcano Infrasonic Crater Resonance). https://doi.org/10.5281/zenodo.3235683

Watson, L. M., Dunham, E. M., & Johnson, J. B. (2019). Simulation and inversion of harmonic infrasound from open-vent volcanoes using an efficient quasi-1D crater model. *Journal of Volcanology and Geothermal Research*, *380*, 64–79. https://doi.org/10.1016/j.jvolgeores.2019.05.007

Witsil, A. J., & Johnson, J. B. (2018). Infrasound explosion and coda signal investigated with joint analysis of video at Mount Erebus, Antarctica. *Journal of Volcanology and Geothermal Research*, *357*, 306–320. https://doi.org/10.1016/j.jvolgeores.2018.05.002

Woods, A. W., & Bower, S. M. (1995). The decompression of volcanic jets in a crater during explosive volcanic eruptions. *Earth and Planetary Science Letters*, *131*(3–4), 189–205. https://doi.org/10.1016/0012-821X(95)00012-2